Optics and Lasers in Engineering 134 (2020) 106279

Contents lists available at ScienceDirect

Optics and Lasers in Engineering

journal homepage: www.elsevier.com/locate/optlaseng

# Super resolution laser line scanning thermography

S. Ahmadi [a,*], P. Burgholzer [b], P. Jung [c], G. Caire [c], M. Ziegler [a]

[a] Bundesanstalt für Materialforschung und -prüfung (BAM), Berlin 12200, Germany
[b] Research Center for Non Destructive Testing, Linz 4040, Austria
[c] TU Berlin, Communications and Information Theory, Berlin 10587, Germany

ARTICLE INFO

*Keywords:*
Super resolution
Laser thermography
Compressed sensing
Laser scanning
Joint sparsity

ABSTRACT

In this paper we propose super resolution measurement and post-processing strategies that can be applied in thermography using laser line scanning. The implementation of these techniques facilitates the separation of two closely spaced defects and avoids the expected deterioration of spatial resolution due to heat diffusion.

The experimental studies were performed using a high-power laser as heat source in combination with pulsed thermography measurements (step scanning) or with continuous heating measurements (continuous scanning). Our work shows that laser line step scanning as well as continuous scanning both can be used within our developed super resolution (SR) techniques. Our SR techniques make use of a compressed sensing based algorithm in post-processing, the so-called iterative joint sparsity (IJOSP) approach. The IJOSP method benefits from both - the sparse nature of defects in space as well as from the similarity of each measurement. In addition, we show further methods to improve the reconstruction quality e.g. by simple manipulations in thermal image processing such as by considering the effect of the scanning motion or by using different optimization algorithms within the IJOSP approach. These super resolution image processing methods are discussed so that the advantages and disadvantages of each method can be extracted.

Our contribution thus provides new approaches for the implementation of super resolution techniques in laser line scanning thermography and informs about which experimental and post-processing parameters should be chosen to better separate two closely spaced defects.

## 1. Introduction

Due to its diffuse nature, heat propagation in thermography imposes a spatial resolution limit that is difficult to circumvent. Nevertheless, some approaches have already been investigated that try to break through this spatial resolution limit, e.g. the use of virtual waves, which offer 3D image reconstruction and a higher signal-to-noise ratio than thermal waves [1,2]. Moreover, structured heating has been used for resolving defects more accurately [3]. Methods like laser line scanning thermography [4] exhibit fast data acquisition and are attractive for industrial applications, but suffer from the degrading effect of heat diffusion in terms of defect detectability.

SR laser scanning has already attracted great interest in fields of structured illumination microscopy where also scanning patterned illumination has been used to enhance the spatial resolution significantly [5,6]. Apart from optical SR, also software based SR image processing gains more and more attention even in the field of thermography [7] where sub-pixel image localization could be shown based on sub-pixel camera position shifts. The main challenge in this technique is the exact determination of the camera position [8]. Therefore, in our work, we show a way to process the data without knowing the exact positions and to use the position shifts with the laser source instead of the camera resulting in blind SR laser scanning.

In our recent work we have already shown that the application of photothermal SR techniques can enhance the spatial resolution limit by using pseudo-random blind illumination patterns with a laser array and the IJOSP approach in post-processing [9]. The combination of laser scanning [10,11] with SR techniques could be of particular interest for industrial applications, as it offers the possibility to monitor the resulting heat propagation from laser heating with a high resolution. An irregular heat propagation could be recognized and leads to indications of defects.

Metallic samples have a high thermal conductivity and high thermal diffusivity. Therefore, to follow the heat flow in these metallic samples, after laser excitation, high camera frame rates of the infrared (IR) camera are necessary. Now, measuring a thermal film sequence over 15 minutes in high definition with a high frame rate results in big data sets. Since the IJOSP algorithm, which is used in our SR techniques, is not performant enough to process such a big data set, one can reduce the data size of the film sequence for example by simply extracting the

* Corresponding author.
*E-mail address:* samim.ahmadi@bam.de (S. Ahmadi).

https://doi.org/10.1016/j.optlaseng.2020.106279
Received 8 April 2020; Received in revised form 5 June 2020; Accepted 14 June 2020

maximum thermogram of each measurement inside the long thermal film sequence [12].

In this paper we show how to implement different SR strategies for laser scanning and highlight the effect of the experimental design as well as of certain image post-processing methods. Different laser scanning methods like step scanning and continuous scanning are described, as both methods require different experimental and post-processing strategies to achieve the highest reconstruction quality. The basis for outperforming conventional thermographic evaluation methods is to perform multiple measurements with a slight position shift enabling optical super resolution. This allows for a combination with compressed sensing (CS) based algorithms which benefit from multiple measurements in a jointly sparse regime and is discussed in details in this work.

Regarding experimental parameters, we studied the influence of choosing different laser pulse lengths for step scanning and homogeneous illumination, different laser line widths for step and continuous scanning as well as different scanning velocities for continuous scanning. In post-processing we require the thermographic point spread function (PSF) [13] to make use of our CS based algorithm called IJOSP. Since the shape of the thermographic PSF will be modified using different velocities in the continuous scanning technique, this should be taken into account. Further, the effect of choosing the regularization parameter within the IJOSP algorithm will be discussed. Finally our work shows different ways for implementing IJOSP in order to make use of the joint sparsity property, so that higher reconstruction qualities are reached with a higher probability.

## 2. Methodology

### 2.1. Experiment

Fig. 1 shows a graphical explanation of step scanning and continuous scanning and a conventional homogeneous illumination, respectively.

It can be seen that the step scanning includes a cooling process after each measurement for one position which implies that pulsed thermography measurements are used in the step scanning strategy. In contrast, the continuous laser scanning method shows continuous heating while moving the specimen constantly with a certain velocity until the end of the specimen is reached.

Fig. 2 shows the experimental setup that has been used to investigate the SR techniques for laser line scanning.

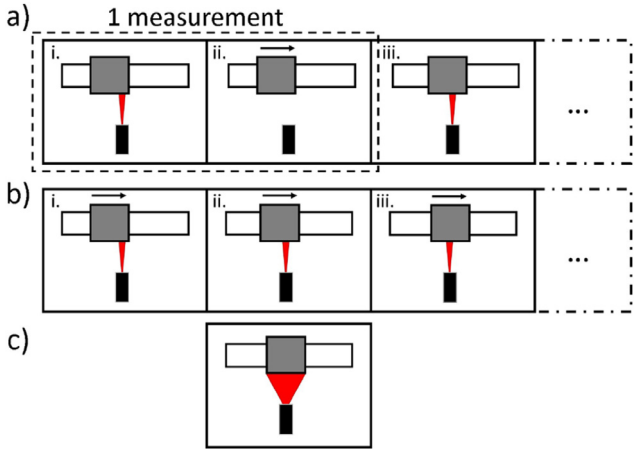


**Fig. 1.** Different laser line scanning strategies: a) step scan: i. laser pulse, ii. let the specimen cool down and move the specimen with the translation stage to the next position, iii. start the next measurement by using again the laser pulse, but now for a different position; b) continuous scan: illuminating the specimen with the laser while moving the specimen with the translation stage with a certain velocity, c) homogeneous illumination: laser illuminates the whole front surface of the specimen.

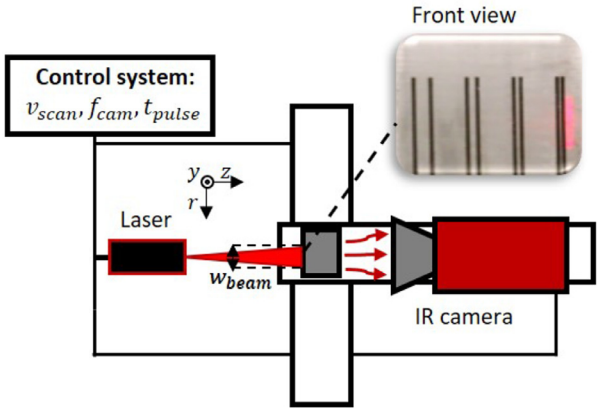


**Fig. 2.** The experimental data was measured with an IR camera (Infratec IR9300, $f_{cam} = 100$ Hz, full frame: 1280 x 1024 pixel) in transmission configuration. A high-power laser was used (maximum output power $P_{\max} = 500$ W, $\lambda = 930 - 950$ nm). The front view (illuminated side of the sample) shows a real measurement with a certain laser line width (see the red line on the right side of the front view picture). The control system controls the translation stage where the specimen and the IR camera are moved along the vertical translation axis. The control system consists of a computer connected with an embedded device (National Instrument MyRIO 1900). The connection lines represent the cable paths. The black lines on the front surface of the investigated specimen were engraved by a laser and serve as absorption lines for the laser beam. The material of the specimen is steel S235JR. The distances between the absorption lines are 0.5, 1, 2 and 4 mm, respectively. An absorption line has a width of 1 mm. The thickness of the specimen is given by 4 mm. The distance between the absorption line pairs and to the edge of the sample from the first and last absorption pair is 10 mm. This setup represents the illumination with a single laser line which belongs to a measurement shown in Fig. 1 a) or b). (For interpretation of the references to colour in this figure legend, the reader is referred to the web version of this article.)

In order to compare all the experiments which have been performed, the irradiance has always been adjusted according to the variation of the pulse length $t_{pulse}$ in the step scanning and homogeneous illumination experiments, of the laser line width $w_{beam}$ in the step and continuous scanning experiments and of the scanning velocity $v_{scan}$ in the continuous scanning experiments. Consequently, the measured data was in the same temperature range for different measurement configurations (around 3 – 5 K temperature rise by excitation).

Step scanning was performed by moving the specimen with a fraction of the laser line width. The moving distance should be smaller than the laser line width such that we have measurements with a certain overlap so that we can benefit from the joint sparsity property within the IJOSP algorithm.

### 2.2. Mathematical description of the measured data

The image processing was performed in Matlab. After importing the data, the loaded thermograms were converted to arrays by using the mean over the vertical pixels in the region of interest. An exemplary conversion is shown in Fig. 3.

Calculating the mean over the pixels along the vertical axis as shown in Fig. 3 results in the matrix of measured temperature values $T_{meas} \in \mathbb{R}^{N_r \times N_t}$. The variable $r$ stands for the position in the horizontal axis with $r = k_r \cdot \Delta r_{cam} = [1 \dots N_r] \cdot \Delta r_{cam}$ and $t$ for the time with $t = k_t \cdot \Delta t_{cam} = [1 \dots N_t] \cdot \Delta t_{cam}$, whereby $\Delta t_{cam} = f_{cam}^{-1}$ represents the time resolution and $\Delta r_{cam}$ stands for the spatial resolution. Thus, sampled values can be described by $T_{meas}[r,t] = T_{meas}(k_r \cdot \Delta r_{cam}, k_t \cdot \Delta t_{cam})$, whereby the round brackets designate a continuous function and squared brackets designate discrete values, respectively. We measured with a spatial resolution of $\Delta r_{cam} = 54\ \mu m$ which indicates that we cover with one camera pixel an area of $A_{px} = (54\ \mu m)^2$. However, the step scanning strat-

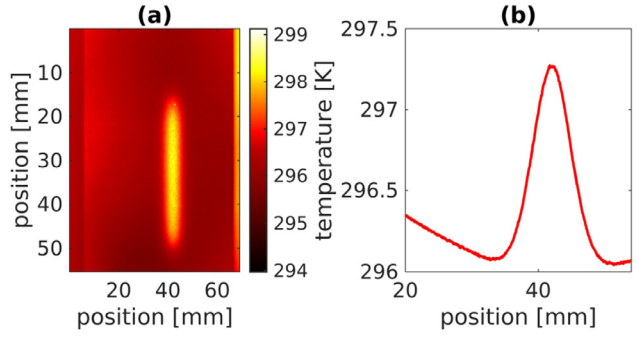


**Fig. 3.** Elimination of dimension y by calculating the mean over the vertically arranged pixels: a) shows an exemplary measured thermogram, b) represents the corresponding mean over the pixels around the temperature rise of a).

egy requires different measurements as described in Fig. 1. For this reason the matrix changes only for the step scan case to $T^m_{meas,step}[r,t]$ with $T^m_{meas} \in \mathbb{R}^{N_r \times N_t}$ and $m = 1 \dots N_{meas}$, whereby $m$ stands for the measurement number. In the following $T_{meas}$ designates temperature differences such that $T[r,t] = T_0[r] + T_{meas}[r,t]$, whereby $T$ stands for the absolute measured temperature value and $T_0$ for the initial measured temperature.

Taking into account the calculation of the average value over the vertically arranged pixels in y-direction (see y-direction shown in Fig. 2), the underlying physics in the experiment can be described mathematically as follows [14]:

$$T^m_{meas}[r,t] = (\phi_{PSF} *_{r,t} x^m)[r,t] \tag{1}$$

with $x^m[r,t] = I^m[r,t] \cdot a[r]$ for a separable $I^m[r,t] = I^m_r[r] I_t[t] = (\delta^m_r *_r I_{s,r})[r](\delta_t *_t I_{s,t})[t] = (I^m_r \otimes I_t)[r,t]$. $\phi_{PSF} \in \mathbb{R}^{N_r \times N_t}$ stands for the thermal point spread function which is calculated by the Green's function as a fundamental solution of the heat diffusion equation for a point source. $x^m \in \mathbb{R}^{N_r \times N_t}$ describes the product of the illumination pattern $I^m \in \mathbb{R}^{N_r \times N_t}$ and the absorption pattern $a \in \mathbb{R}^{N_r \times 1}$ (see black lines on the front surface of the investigated specimen in Fig. 2) for each measurement $m$ so that $x^m$ designates the absorbed energy from illumination. $I_{s,r} \in \mathbb{R}^{N_r \times 1}$ and $I_{s,t} \in \mathbb{R}^{N_t \times 1}$ are shape functions referring to the laser radiation in spatial and time domain, respectively. The shapes of these functions are determined by the choice of the laser line width in spatial domain and the laser pulse length (for step scanning and homogeneous illumination) in time domain. $I^m_r \in \mathbb{R}^{N_r \times 1}$ and $I_t \in \mathbb{R}^{N_t \times 1}$ are almost equal to the shape functions, but differ due to a space or time shift realized by the convolution with the Dirac delta functions $\delta^m_r \in \mathbb{R}^{N_r \times 1}$ and $\delta_t \in \mathbb{R}^{N_t \times 1}$ which designate the illuminated position in space and time, respectively. The operator $\otimes$ stands for a tensor product and $*$ for a convolution (in space: $*_r$, in time: $*_t$, in space and in time: $*_{r,t}$). With this knowledge we can continue the notation of Eq. (1) by

$$\begin{aligned} T^m_{meas}[r,t] &= (\phi_{PSF} *_{r,t} x^m)[r,t] \\ &= \Big(\phi_{PSF} *_{r,t} \underbrace{[(I^m_r \otimes I_t) \circ (a \otimes 1)]}_{x^m_{line}}\Big)[r,t] \\ &= (\phi_{PSF} *_{r,t} x^m_{line})[r,t], \end{aligned} \tag{2}$$

whereby $\circ$ stands for the Hadamard-product. Thus, $x^m_{line}$ considers the influence of the laser line width as well as of the laser pulse length.

In this paper we make use of the CS based IJOSP approach. According to the well-known compressed sensing theory [15,16], we obtain the highest reconstruction quality within the IJOSP approach if $x$ is as sparse as possible and $\phi$ has a high mutual incoherence. This is actually given by choosing $\phi$ as a line spread function where the laser line width and pulse length are considered. For this reason the equations in (2) can be rewritten as follows:

$$\begin{aligned} T^m_{meas}[r,t] &= (\phi_{PSF} *_{r,t} x^m)[r,t] \\ &= \Big(\phi_{PSF} *_{r,t} \big[(\delta^m_r *_r I_{s,r}) \otimes (\delta_t *_t I_{s,t})\big] \circ (a \otimes 1)\Big)\Big)[r,t] \\ &= \Big(\underbrace{\Big(\phi_{PSF} *_{r,t} [I_{s,r} \otimes (\delta_t *_t I_{s,t})]\Big)}_{\phi_{line}} *_r \underbrace{(\delta^m_r \circ a)}_{x^m_\delta}\Big)[r] \\ &= (\phi_{line}[\cdot,t] *_r x^m_\delta[\cdot])[r]. \end{aligned} \tag{3}$$

The Eqs. (1) - (3) are valid for step scanning, but can be simply rewritten for continuous scanning. Based on the aforementioned Eq. (3) and the different experimental scanning strategies, the mathematical model for the performed measurements can be stated as follows:

$$\begin{aligned} T^m_{meas,step}[r,t] &= \big(\phi_{line,step}[\cdot,t] *_r x^m_{\delta,step}[\cdot]\big)[r] \\ T_{meas,cont}[r,t] &= \big(\phi_{line,cont}[\cdot,t] *_r x_{\delta,cont}[\cdot,t]\big)[r] \\ T_{meas,homog}[r,t] &= \big(\phi_{line,homog}[\cdot,t] *_r x_{\delta,homog}[\cdot]\big)[r] \\ x^m_{\delta,step}[r] &= I^m_{\delta,step}[r] \cdot a[r] \\ x_{\delta,cont}[r,t] &= I_{\delta,cont}[r,t] \cdot a[r] \\ x_{\delta,homog}[r] &= I_{\delta,homog}[r] \cdot a[r]. \end{aligned} \tag{4}$$

Since $\phi_{line}$ considers the physical properties of the used laser line such as the laser pulse length and laser line width, it can be rather described as a thermal line spread function (LSF).

The LSF for continuous scanning contains the variation of the velocity and does not include the pulse length [17,18]. Since we are interested in the reconstruction of the defects which can be described by the quantity $a$, our initial goal is to obtain the unknown variable $x$. The equations in (4) show that $x$ varies depending on the used method due to varying illumination pattern. In step scanning the illumination pattern differs for each measurement $m$ because for each measurement $m$ a different position is illuminated. In continuous scanning the illumination pattern differs due to the motion of the laser, which leads to a time dependence of the illumination pattern. In the homogeneous illumination method the illumination pattern neither depends on the measurement number nor on the time since there is no position shift or motion involved.

$T_{meas}$ is known and $\phi_{line}$ can be calculated numerically [12,13]:

$$\begin{aligned} \phi_{line,step/homog}(r, z = L, t) = \frac{2}{4\pi\alpha\rho c_p} \cdot \int_0^t \int_{-\infty}^{\infty} I_{s,r}(r - \tilde{r}) I_t(t - \tilde{t}) \\ \cdot e^{-\frac{\tilde{r}^2}{4\alpha\tilde{t}}} \cdot \sum_{n=1}^{\infty} R^{2(n-1)} e^{-\frac{(2n-1)^2 L^2}{4\alpha\tilde{t}}} d\tilde{r} \frac{d\tilde{t}}{\tilde{t}} \end{aligned} \tag{5}$$

The above shown formula for $\phi$ considers the laser pulse length (convolution in time with the variable t) and the laser line width (convolution in space with the variable r). $\rho$ stands for the mass density, $c_p$ for the specific heat, $\alpha$ for the thermal diffusivity, $R$ for the thermal reflectance from the material to air, and $L$ for the thickness of the specimen. Since we investigated steel S235JR, we have used the following values for the material parameters: $\rho = 7800$ kg/m$^3$, $c_p = 440$ J/kg/K, $\alpha = 1.6 \cdot 10^{-5}$ m$^2$/s and $R = 1$. The Eq. (5) can be used for step scan and homogeneous illumination, the difference of the calculation of $\phi_{step}$ and $\phi_{homog}$ is the laser line width $w_{beam}$. $\phi_{cont}$ looks different due to the missing convolution in time with the laser pulse length since there is no real pulse length. The laser is continuously switched on so that $I_t$ can be neglected. Therefore, we have used the following $\phi_{cont}$ [18]

$$\begin{aligned} \phi_{line,cont}(r, z = L, t) = \frac{2}{4\pi\alpha\rho c_p} \cdot \int_0^t \int_{-\infty}^{\infty} I_{s,r}(r - \tilde{r}) \cdot e^{-\frac{(\tilde{r} - v \cdot \tilde{t})^2}{4\alpha\tilde{t}}} \\ \cdot \sum_{n=1}^{\infty} R^{2(n-1)} e^{-\frac{(2n-1)^2 L^2}{4\alpha\tilde{t}}} d\tilde{r} \frac{d\tilde{t}}{\tilde{t}} \end{aligned} \tag{6}$$

Eq. (6) now considers the motion by adding $v \cdot t$ in the exponential term. Further, the integration over time considers the superimposed influence of the heating from the previous time steps.

Fig. 4 shows different shapes for the LSF $\phi_{line}$. The figure shows how the experimental parameters - the laser pulse length and the laser line width - influence the Gaussian shape of $\phi$.

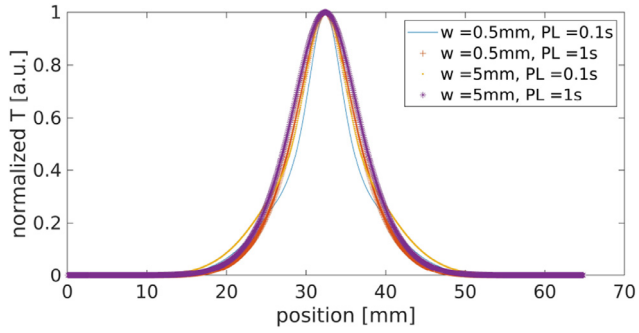


**Fig. 4.** Different shapes of the line spread function $\phi$ are shown over position $r$ as normalized temperature values, normalized by the maximum temperature amplitude. We varied the laser pulse length and laser line width.

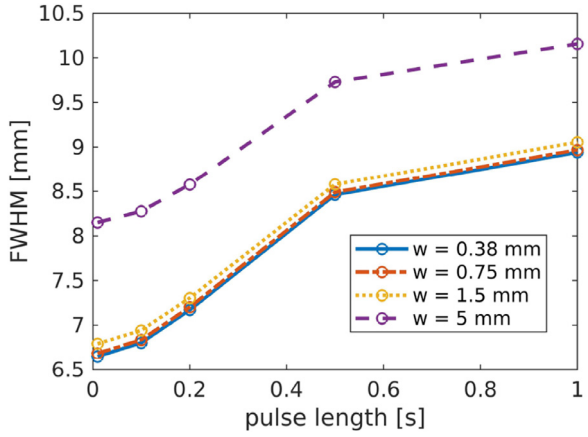


**Fig. 5.** The FWHM is plotted over the variation of the laser pulse length. We have calculated the FWHM for five different pulse lengths and interpolated the calculated values. It can be observed that a small laser pulse length as well as a small laser line width results in a small FWHM of the used thermal PSF for the super resolution studies.

In this paper work we are also studying the effect of choosing different scanning velocities in continuous scanning on our SR techniques. Therefore, in Fig. 6 we show the shape variation of the thermal LSF depending on the chosen scanning velocity.

The Figs. 4, 5 and 6 indicate the extent of the effect in the variation of the experimental parameters. Thus, a change in the scanning velocity brings a strong asymmetry into the Gaussian profile. Furthermore, for smaller scanning velocities we can see a high influence by the superposition of the previously heated regions from the previous time steps. Higher scanning velocities lead to a stronger shift of the temperature maximum.

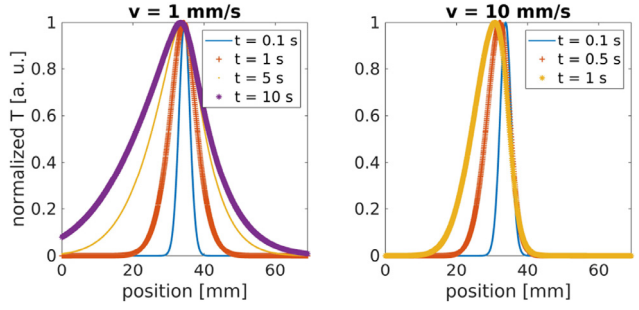


**Fig. 6.** In this image two diagrams for different scanning velocities are shown. In each of both diagrams we varied the time step to observe the shape change of the thermal LSF.

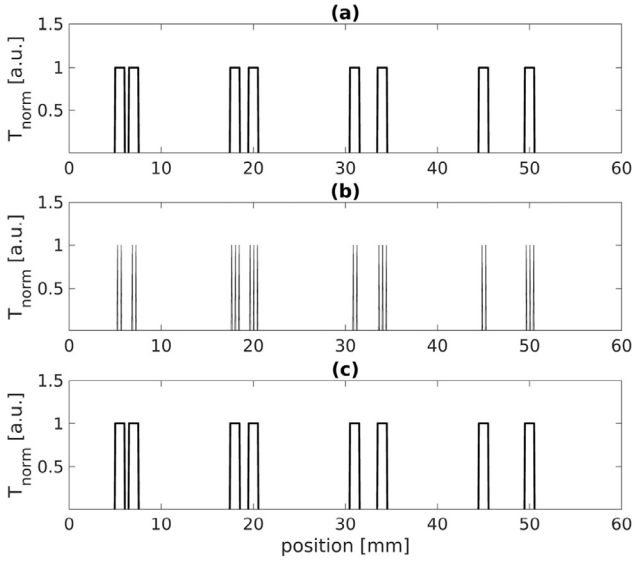


**Fig. 7.** (a) the absorption or defect pattern $a$, (b) $\sum_m(x_\delta^m) = \sum_m(\delta_r^m \circ a)$ and (c) $\sum_m(x_{LW}^m) = \sum_m(I_r^m \circ a)$. These diagrams have been created on the basis of the chosen experimental parameters so that we have used a position shift of 0.4 mm between each measurement $m$ and a laser line width of around 0.4 mm which leads to the fact that considering the laser line width in $x$ with $x_{LW}$ enables to reconstruct the absorption pattern $a$ much better than with $x_\delta$.

In Fig. 6 it can be observed that the change in the shape of the thermal LSFs becomes smaller for higher time steps. This means that a quasi-static level can be reached after a certain time where the shape of the thermal LSF does not change for further time steps.

### 2.3. Image processing based on SR laser line scanning

The results in Section 3 (step scanning and continuous scanning) were generated by using a $\phi$ which does not consider the laser line width so that the laser line width is still in the solution $x$, more precisely - according to the equations in (4) - in the illumination pattern $I$. Thus, we have used the following mathematical description in our implementation:

$$\begin{aligned} T_{meas}^m[r,t] &= (\phi_{PSF} *_{r,t} x^m)[r,t] \\ &= \left(\phi_{PSF} *_{r,t} [(I_r^m \otimes I_t) \circ (a \otimes 1)]\right)[r,t] \\ &= \Bigg(\underbrace{\left((\phi_{PSF}[r,\cdot] *_t I_t[\cdot])[t]\right)}_{\Phi_{PL}} *_r \underbrace{\left(I_r^m \circ a\right)}_{x_{LW}^m}\Bigg)[r] \\ &= (\phi_{PL}[\cdot,t] *_r x_{LW}^m[\cdot])[r], \end{aligned} \tag{7}$$

whereby $PL$ stands for pulse length in time domain and $LW$ for the laser line width in spatial domain. The reason for rewriting $\phi_{line}$ to $\phi_{PL}$ in the implementation is that choosing $\phi_{line}$ results in $x_\delta$ which is based on Dirac delta peaks in space. These Dirac delta peaks have a distance of the position shift which is much larger than our measured spatial resolution ($54\mu$ m) that defines the width of a Dirac delta peak. Hence, it is not possible to reconstruct an absorption line with a certain width perfectly using $\phi_{line}$. In contrast, calculating with $\phi_{PL}$, it would be possible to reconstruct the absorption line much more accurate since the solution $x_{LW}$ considers the laser line width which is even for our studies with the smallest laser line width around 0.4 mm and therefore larger or as large as the position shift. Thus, using $\phi_{PL}$ enables to reconstruct the absorption lines perfectly (see Fig. 7 (b) vs (c) for better understanding).

#### 2.3.1. Realization of a framework for the IJOSP approach

As explained in details in Ref. [12] different reconstruction techniques can be used to obtain a sparse representation of the measured

data. The step scanning method requires such a method, otherwise we can not apply the IJOSP approach in a performant manner. Using such a reconstruction technique before applying IJOSP allows for calculations under one minute with our computer for the IJOSP approach. Otherwise the calculations would take more than one hour.

We applied the simplest reconstruction technique - the extraction of the maximum thermogram from the IR camera film. Extracting the maximum thermogram for each measurement in the step scanning data enables to reduce the data size by a factor of 2000 since we measured 2000 frames per measurement. Consequently, we obtain $T^m_{rec,step}[r]$ with $T^m_{rec,step} \in \mathbb{R}^{N_r \times 1}$. We also apply the maximum thermogram method as data reduction technique to the matrix $\phi_{PL,step}$ so that we obtain $\phi_{rec,step}$ and eliminate the time dimension. In the following we write $T_{rec,step}[r, m]$ instead of $T^m_{rec,step}[r]$ and $x_{LW,step}[r, m]$ instead of $x^m_{LW,step}[r]$. Further, we determined a $\phi_{rec,cont}$ by choosing a very high time stamp $t_0$ with $\phi_{rec,cont}(r) = \phi_{cont}(r, t = t_0)$. A very high value for $t_0$ is necessary since we are reaching after a certain time $t_{qs}$, the - in the previous subsection already described - quasi-static level. Based on this knowledge, in our studies we decided to take $t_0 = 20\,s$, where we definitely reached the quasi-static level.

IJOSP relies on the compressed sensing principle. Our above mentioned mathematical description leads to the following IJOSP framework:

$$\begin{aligned} T_{rec,step}[r, m] &= \big(\phi_{rec,step}[\cdot] * x_{step}[\cdot, m]\big)[r] \\ T_{rec,cont}[r, t] &= \big(\phi_{rec,cont}[\cdot] * x_{cont}[\cdot, t]\big)[r] \end{aligned} \tag{8}$$

The equations in (8) exhibit great similarity due to the aforementioned transformations. If one now equates the variable m with the variable t, the same equations would be used to describe the data from step and continuous scanning.

The quantity T is given by the measured data for each scanning strategy, respectively. T was already described in the Eqs. (4) and (8) and is shown in Fig. 8 for all scanning strategies.

### 2.3.2. Application of the IJOSP approach

The IJOSP approach tries to find a solution $\hat{x}$ in the following minimization problem [19,20]:

$$\begin{aligned} \min_{\hat{x}} \tfrac{1}{2} \sum_{m=1}^{N_{meas}} \sum_{k=1}^{N_r} \Big| \big(\phi_{rec}[\cdot] * \hat{x}[\cdot, m]\big)[r_k] - T[r_k, m] \Big|^2 \\ + \lambda_1 \|\hat{x}\|_{2,1} + \tfrac{\lambda_2}{2} \|\hat{x}\|_2^2, \end{aligned} \tag{9}$$

where $\phi$ can be replaced by $\phi_{rec,step}$ or $\phi_{rec,cont}$, $\hat{x}$ is the solution of the optimization algorithm which ideally equals $x$. $\hat{x}$ and T can also be replaced by $\hat{x}_{LW,step}$ or $\hat{x}_{LW,cont}$ and $T_{rec,step}$ or $T_{rec,cont}$, respectively. Two regularizers are involved in the minimization problem that are controlled by the regularization parameters $\lambda_1$ and $\lambda_2$ which control the impact of block sparsity $\|\hat{x}\|_{2,1} = \sum_{k=1}^{N_r} \sqrt{\sum_{m=1}^{N_{meas}} |\hat{x}[r_k, m]|^2}$ and Tikhonov regularization $\|\hat{x}\|_2^2$.

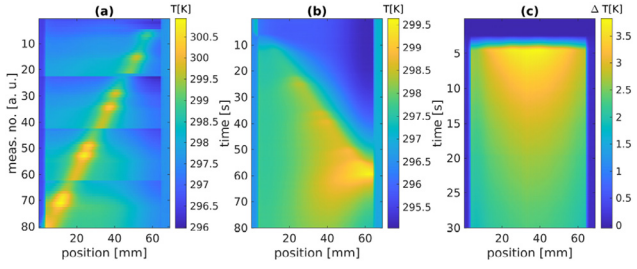


**Fig. 8.** a) $T_{rec}$ from step scan: Here, we have used $w_{beam} = 1.5$ mm and $t_{pulse} = 1$ s. To reduce the measurement time we decided to perform a high position shift between two defect pairs. Since we investigated four defect pairs, we had to perform three high position shifts. These are recognized by the three cuts in the image at measurement number (no.) 23, 43 and 63 since we performed about 20 measurements for each defect pair. The first measurements were taken at around 60 mm, so that the position was shifted towards the position 0 mm. b) $T_{meas}$ from continuous scan: $w_{beam} = 1.5$ mm, $v_{scan} = 1$ mm/s, the laser line movement starts from 0 mm and ends at around 60 mm. c) $T_{meas}$ from homogeneous illumination (square): $A_{beam} = 60 \times 60$ mm$^2$, $t_{pulse} = 2$ s.

The IJOSP approach is not suitable for the data generated by the homogeneous illumination or does not lead to an improvement compared to the other two methods. The reason is that it is only one measurement with complete illumination of the surface, so that the joint sparsity of different measurements cannot be exploited by the position shift or the movement like in step or continuous scanning.

In our studies we solved the minimization problem in Eq. (9) using the Block-Fast Iterative Soft Thresholding Algorithm (FISTA) which does not make use of the Tikhonov regularization and the Block-Elastic-Net algorithm [14,21] which does. Since FISTA and the Elastic-Net algorithm both use a gradient-based optimization, a step size L can be chosen. In fact we update our solution within the iterative optimization with the factor $2/L$, whereby the factor 2 comes from the calculation of the derivative. This means that L (the Lipschitz constant) is rather a quantity standing for the step size resolution since the step size decreases with increasing L, but due to simplicity we call L the step size parameter. Thus, we can choose two parameters ($L$ and $\lambda_1$) for FISTA or three parameters for the Elastic-Net approach ($L$, $\lambda_1$ and $\lambda_2$) which have an influence on our result.

### 2.4. Methods to improve the reconstruction quality

In our work we found interesting ways to improve the reconstruction quality of our measured data and tried to investigate the following points to achieve the highest reconstruction quality:

1. Choose the optimal experimental parameters for the laser line width, pulse length for step scanning, camera frequency and scanning velocity for continuous scanning
2. Choose suitable parameters in the Block-FISTA approach for $L$ and $\lambda_1$ or in the Block-Elastic-Net approach where we have to choose $\lambda_2$, too
3. Consideration of motion in continuous scanning: Variation of the thermal LSF

In order to investigate the influence of the experimental and post-processing parameters we varied all mentioned parameters in 1. and 2. to figure out the best configuration for the application of the IJOSP approach.

The consideration of the motion can be important for higher velocities since the shape of the LSFs changes significantly according to Eq. (6) as one can see in Fig. 4.

## 3. Results and discussion

### 3.1. Determination of the reconstruction quality

For a fair comparison of each result after applying the IJOSP algorithm to all measurement data sets with the corresponding variation of the experimental parameters as well as the regularization parameters in the Block-FISTA algorithm [20], a reconstruction quality factor is introduced as the variable "rq". The reconstruction quality can be calculated by the following formula [12]:

$$rq = \begin{cases} \dfrac{max(\hat{x} \star x)}{max(x \star x)} & \text{if } (N_{peaks} \geq 8) \ \wedge \ (N_{peaks} \leq 16) \\ 0 & else \end{cases} \tag{10}$$

whereby $\star$ stands for the cross-correlation and rq is a number in [0,1]. To get a better idea of how $\hat{x}$ can look like, one can have a look at the IJOSP/ Block-FISTA result in Fig. 9 after structured SR heating.

Using the cross-correlation for the determination of the reconstruction quality can lead to false conclusions e.g. if the IJOSP result $\hat{x}$ exhibits 100 narrow peaks with a small FWHM compared to the width of

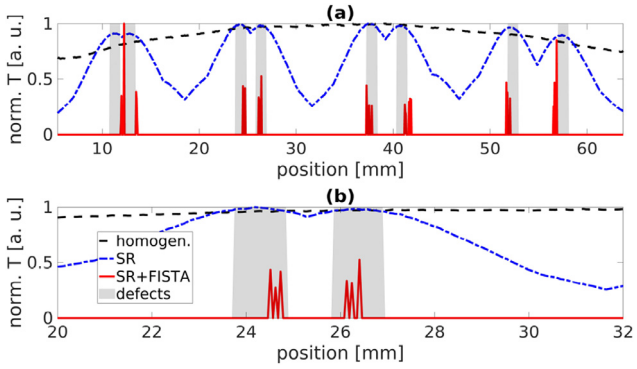


**Fig. 9.** These results refer to step scan measurements. The curve designated by homogen. describes the calculated mean over the time from the homogeneous illumination measurement (see Fig. 8 (c)). SR refers to the result from applying our super resolution structured heating and calculating the maximum values for each measurement of $T_{rec}$ (see Fig. 8 (a)). An additional application of IJOSP using Block-FISTA as optimizer results in the red solid curve. The defects are standing for the absorption lines on the front surface of our investigated specimen. The diagram in (b) is just a zoom from diagram (a). (For interpretation of the references to colour in this figure legend, the reader is referred to the web version of this article.)

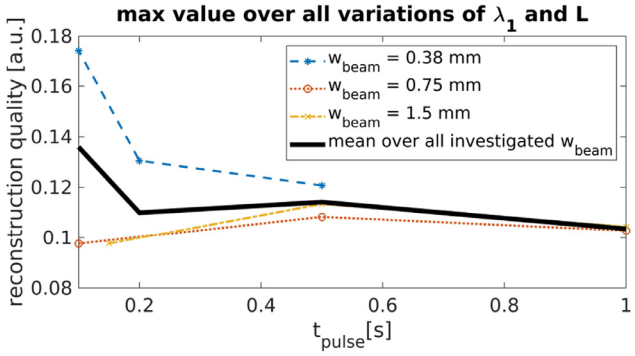


**Fig. 10.** The reconstruction quality is plotted over the laser pulse length for different laser line widths. In addition, the mean over all laser line widths is shown. We determined the reconstruction quality values by calculating the maximum rq value over all variations of $\lambda_1$ and $L$ using Block-FISTA within the IJOSP approach.

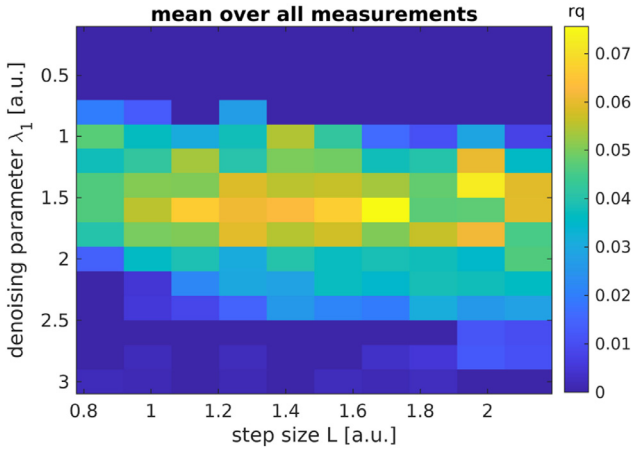


**Fig. 11.** Investigation of the influence choosing different post-processing parameters within the Block-FISTA routine on the reconstruction quality (shown in colors). Here, the mean rq value over all measurements was calculated for each parameter pair.

one absorption line and some of them are in the region of the absorption lines. This leads to high rq values although there are many peaks detected outside the region of interest. Therefore, we decided to introduce peak detection boundaries so that we reduce the probability of false conclusions for calculating with the cross-correlation function. We took as lower boundary eight peaks due to the fact that we have four absorption line pairs and as upper boundary 16 because it is possible that we obtain as IJOSP result for example two peaks in the region of one absorption line. Obtaining more than one peak in the region of one absorption line is reasonable since we are using very slight position shifts and use more than one measurement where we illuminate the same absorption line. Therefore, our algorithm detects only peaks with a minimum distance between each other of at least one position shift. Moreover, the number of measured peaks depends on the area covered by one camera pixel.

### 3.2. Comparison of rq values

Before comparing the rq values for step and continuous scanning, it should be noted that we were not able to use the homogeneous illumination technique to resolve the investigated absorption lines (see Fig. 9).

#### 3.2.1. Results for step scan

To perform our SR studies we investigated three different laser line widths $w_{beam} = 0.38, 0.75, 1.5$ mm and different laser pulse lengths in the range $t_{pulse} \in [100, 1000]$ ms. We have chosen these experimental parameters because of our optics equipment which allows us to create laser lines with the aforementioned line widths. The pulse length and the power of the laser were adjusted so that we measure a temperature rise of around 5 K as a maximum measured value in our transmission configuration. We always tried to keep the pulse duration as small as possible to obtain a small FWHM for the thermal LSF.

Furthermore, we varied the post-processing parameters $L \in [0.85, 2.12]$, $\lambda_1 \in [0.2, 3]$ for Block-FISTA or $\lambda_1 \in \{10^{-6}, 10^{-5}, 10^{-4}, 10^{-3}, 10^{-2}, 10^{-1}, 1\}$ and $\lambda_2 \in [0.01, 0.1]$ for Block-Elastic-Net, respectively. The ranges for the parameters $L$, $\lambda_1$ and $\lambda_2$ were chosen individually since we saw realistic results in these range. However, one of these ranges (the range of $\lambda_1$ in Block-Elastic-Net) was chosen for demonstrative reasons. Since both algorithms are based on an iterative optimization and we would like to make the study more comparable, we set for all studies a fixed value for the number of iterations $N_{iter} = 500$. We took this value due to our testing experience, mostly we do not see any more differences after 500 iterations because the convergence has already been achieved.

At first the results for using the Block-FISTA approach are discussed. Fig. 10 shows the obtained results by varying the laser line width and the laser pulse length.

Fig. 10 illustrates the degradation of the reconstruction quality when choosing high pulse lengths as well as high laser line widths. Nonetheless, the differences are not so high since the shape variation of the thermal LSF is also not high which leads to small differences in the FWHM (see Fig. 5 and Fig. 4).

The influence of the post-processing parameters for FISTA is shown in Fig. 11. It can be seen that the reconstruction result is more tolerant regarding the choice of the step size $L$ than regarding the choice of the denoising parameter $\lambda_1$. This is reasonable since $\lambda_1$ serves as a control parameter of the joint sparsity term and therefore thresholds the measured data. Also one can observe that there are certain parameter pairs which can enhance the rq value significantly. Hardly visible, but also reasonable is the slight tendency of better choosing higher values for $\lambda_1$ if one increases the value for $L$. Since we are updating with the factor $2/L$, a higher value for L means a small step which also means that we do not reach our final solution that represents our defects. Using a higher $\lambda_1$ leads to a higher sparsity and threshold sensitivity so that

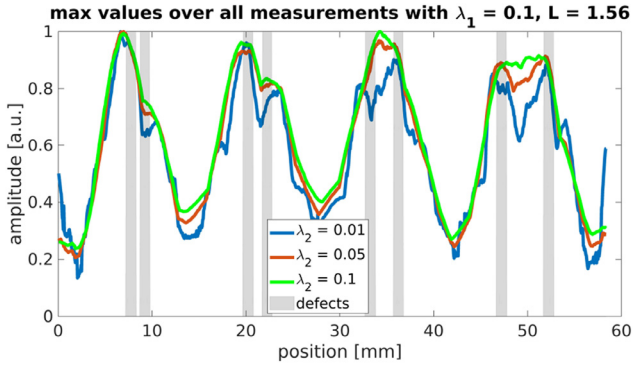


**Fig. 12.** The effect of choosing different values for the Thikonov regularization parameter $\lambda_2$ on the result is shown for a fixed $L$ and $\lambda_1$. The curves were determined by calculating the maximum values over all measurement configurations (different laser line widths and laser pulse lengths).

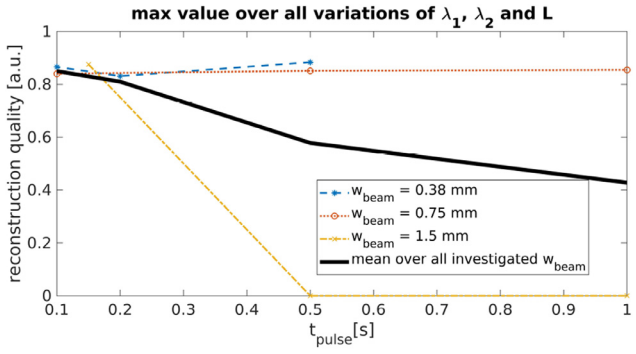


**Fig. 13.** The reconstruction quality is plotted over the laser pulse length for different laser line widths after using Block-Elastic-Net. In addition, the mean over all laser line widths is shown. We determined the reconstruction quality values by calculating the maximum rq value over all variations of $\lambda_1$, $\lambda_2$ and $L$ using Block-FISTA within the IJOSP approach.

we obtain clear peaks as shown in red in Fig. 9 which results in a high reconstruction quality.

To compare the results from Block-FISTA with Block-Elastic-Net, we performed the same parameter studies again. Before showing the results, some different results using Block-Elastic-Net are illustrated in Fig. 12 to understand the following discussion.

The curves in the diagram in Fig. 12 show a high difference compared to the clear peaks which result from applying Block-FISTA (see for comparison the result of Block-FISTA in Fig. 9). The consideration of the Thikonov-regularization with a $\lambda_2 > 0$ decreases the effect of making the result sparse. This can be seen by increasing the value for $\lambda_2$. This diagram shows the importance of the joint sparsity term. To decide which algorithm is better depends on the area of application: Block-FISTA provides clear peaks and an indication that defects exist even with defects which have a distance of 0.5 mm whereas the Block-Elastic-Net perhaps better reconstruct the defect geometries, but struggles to resolve closely spaced defects.

In addition, the new shape of our solution curves from using Block-Elastic-Net can lead to false conclusions after calculating the reconstruction quality according to Eq. (10) since we do have a suitable number of peaks and the curve has a high value over all absorption lines. However, we decided to still use the calculation of the reconstruction quality value according to Eq. (10) to see how the experimental and post-processing parameters influence the quality of the result from Block-Elastic-Net.

Fig. 13 demonstrates the effect of the experimental parameters on the reconstruction quality

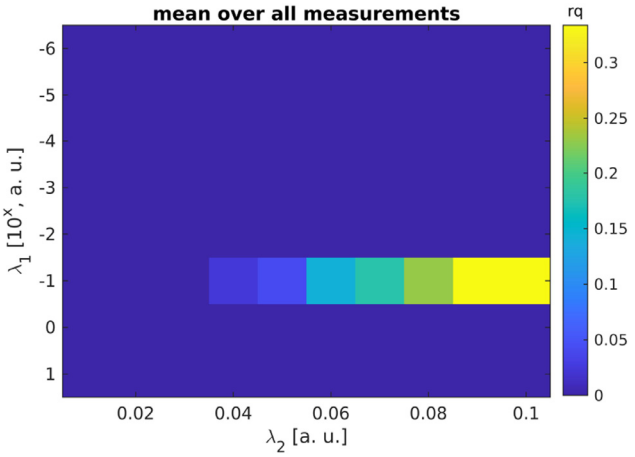


**Fig. 14.** Investigation of the influence choosing different post-processing parameters within the Block-Elastic-Net routine on the reconstruction quality (shown in colors). We calculated the mean rq value over all experimental configurations. The $10^x$ in the y-axis labelling indicates a semi-logarithmic illustration of the data.

The influence of the post-processing parameters on the Block-Elastic-Net result is shown in Fig. 14.

In this figure we varied the denoising parameter $\lambda_1$ with large distances so that we can see how important it is to take the correct $\lambda_1$. Performing these studies takes a lot of time and it is not easy to determine the right value. Although there are algorithms to determine the best suited value such as cross validation or the L-curve method [22,23], these methods do not always provide the best suited value [24]. Apart from that, Fig. 14 further exhibits enhancing rq values for increasing $\lambda_2$. Unfortunately, this result leads to false conclusions as explained before according to Fig. 12 the curve for $\lambda_2 = 0.1$ has a higher rq value than for $\lambda_2 = 0.01$ although the curve for $\lambda_2 = 0.01$ looks better as it indicates better the absorption lines.

### 3.2.2. Results for continuous scan

The continuous scan measurements are much faster than the step scan measurements, but therefore hard to evaluate due to the fact that our heat propagation depends on the scanning velocity.

In our studies we focused on three different scanning velocities: $v_{scan} \in \{10^{-3}, 10^{-2}, 10^{-1}\}$ m/s and took again three different optics for our fiber-coupled laser to realize the three laser line widths as described before. We have adjusted the power of the laser line so that we obtain a comparable maximum value of 5 K temperature rise.

All the results shown in the following have been calculated by using one motion considering thermal point spread function $\phi_{rec,cont}$ which has been calculated according to Eq. (6).

Moreover, we investigated the results generated by using Block-FISTA as optimization with joint sparsity as a prior. The post-processing parameters have been chosen equally to the values and ranges described in the step scan Block-FISTA section.

Fig. 15 shows the mean rq values over all chosen post-processing parameters for different scanning velocities and laser line widths.

The mean rq value tends to be higher for smaller scanning velocities and smaller laser line widths. However, we had a closer look and double checked the results by plotting some results for certain post-processing parameters. We discovered that we are able to resolve practically every absorption line pair with very fast continuous scanning ($v_{scan}$ = 100 mm/s). Fig. 16 shows the result.

According to our calculation of the thermal LSF, one can see from Fig. 6 that the higher the scanning velocity is, the smaller will be the shape variation of the thermal LSF.

With a scanning velocity of $v_{scan}$ = 100 mm/s we obtain a step size of $\Delta r = v_{scan}/f_{cam}$ = 1 mm from one measurement to the next measure-

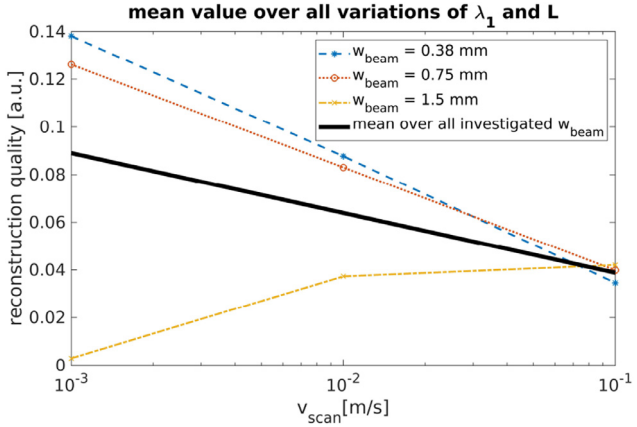


**Fig. 15.** The reconstruction quality is plotted over the scanning velocity for different laser line widths. In addition, the mean over all laser line widths is shown. We determined the reconstruction quality values by calculating the mean rq value over all variations of $\lambda_1$ and $L$ using Block-FISTA within the IJOSP approach.

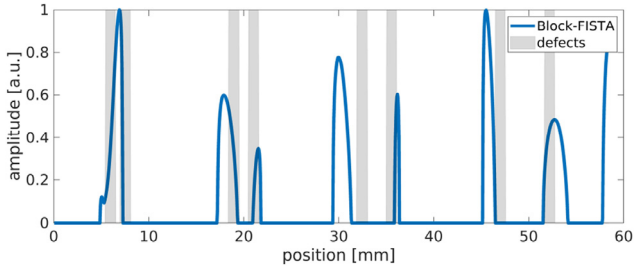


**Fig. 16.** An exemplary plot of the result after applying IJOSP with Block-FISTA on the measured data from very fast continuous scanning for certain parameters: $v_{scan} = 100$ mm/s, $w_{beam} = 0.38$ mm, $\lambda_1 = 1$, $L = 2.1213$.

ment. This means that the thermal LSFs for each time stamp are quite similar and almost independent from each other. For these reasons we obtain clear peaks as shown in Fig. 16. However, it should be noted that this diagram also shows deviations in the positional accuracy for defect reconstruction. This is reasonable since the modeling of $\phi_{cont}$ is much more complex than modeling $\phi_{step}$ due to the motion consideration in $\phi_{cont}$. Using a linear table to move the specimen includes an acceleration and deceleration process which complicates the exact modeling assuming a constant velocity for the whole process. Especially for high scanning velocities as shown in Fig. 16, the acceleration and deceleration process have a big influence since the investigated specimen has only a total length of 60 mm.

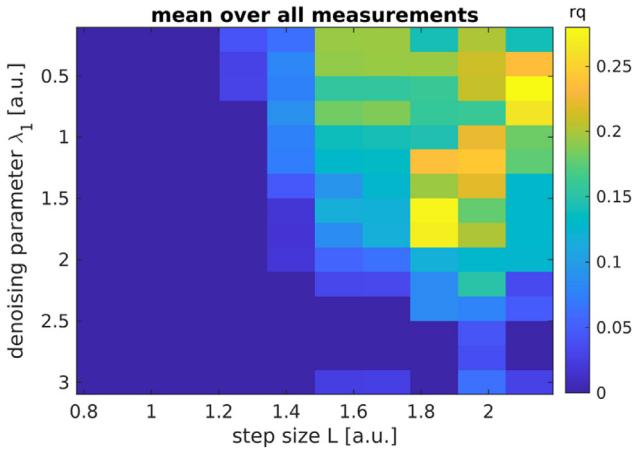


**Fig. 17.** Calculated rq values for a variation of the denoising parameter $\lambda_1$ and the step size $L$. The rq values were determined by calculating the mean over all measurement configurations regarding the variation of the scanning velocity and the laser line width using the Block-FISTA within the IJOSP approach.

For the sake of completeness, Fig. 17 shows the rq values for different values for $\lambda_1$ and $L$.

Fig. 17 does not provide relevant information except for the fact that we rather have to use high values for L and not too high values for $\lambda_1$ to obtain higher rq values.

Finally, it should be noted that we obtain similar results by using a time-dependent thermal LSF for all our studies in terms of continuous scanning without extracting just one LSF. We further studied that the choice for the velocity of the thermal LSF should be quite accurate in order to obtain a high reconstruction quality.

## 4. Conclusion

This paper work discusses how to obtain the optimal reconstruction quality using SR techniques based on laser line scanning. The investigations were mainly focused on experimental parameters such as the laser pulse length for step scanning, the laser line width as well as the scanning velocity for continuous scanning and on post-processing parameters such as the step size $L$, the denoising parameter $\lambda_1$ and the Thikonov control parameter $\lambda_2$ (see Eq. (9)). The resolution improvement is clearly given by a magnification of the SNR realized by the hardware based optical SR and the CS based post-processing. Since the IJOSP algorithm promotes sparse solutions, we will always obtain clear and high SNR based signals. According to Ref. [25] an improvement of the SNR results in a reduction of the corresponding Abbe-limit. Decreasing the Abbe-limit makes also defects with submillimeter distance to each other resolvable.

Our studies show that the reconstruction quality is influenced by each of these methods and parameters. The optimal experimental parameters are given if the laser pulse length as well as the laser line width are chosen as small as possible (one should pay attention that the irradiance is high enough to see an appropriate temperature rise) for step scanning and the scanning velocity for continuous scanning could also be chosen relatively high to obtain a sharp shape for the thermal LSF and therefore clear peaks according to our defects. Further, we could show that the optimal reconstruction is obtained by considering the spatial broadening by the laser line width within the solution $x$ by $x = x_{LW}$ as described in Eq. (7). The choice of the denoising parameter $\lambda_1$ is not intuitive and should be adapted to the noise level of the measurement data. This parameter proved to be critical and it has been difficult to find the parameter that leads to the highest reconstruction quality. Furthermore, it could be shown that a higher value for $\lambda_2$ smoothens our reconstruction result. Also we could demonstrate that the effect of the step size strongly correlates with the choice of $\lambda_1$ and $\lambda_2$ so that all post-processing parameters are connected. Continuous scanning requires an adaption of the thermal PSF which makes the mathematical model more complex, but outperforms step scanning in terms of measurement time (1 second vs 30 minutes). Step scanning data needs to be reduced by methods like extracting the maximum thermogram and eliminating the time dimension since the data size is too high, but benefits from more measurements in terms of positional accuracy in the reconstruction.

In total, our work shows that both methods - step scanning and continuous scanning - are suitable strategies for our so far used SR approach in combination with IJOSP. The combination of a single laser based optical super resolution with IJOSP leads to outstanding results without a need of laser arrays which makes this approach very attractive for industrial applications.

As an outlook, these studies encourage us to find a suitable method to automatically calculate the investigated post-processing parameters. Finally, we are interested in testing our SR techniques on specimens

with internal defects, also in reflection configuration, applying our new gained knowledge about the choice of experimental and post-processing parameters.

## Declaration of interests

The authors declare that they have no known competing financial interests or personal relationships that could have appeared to influence the work reported in this paper.

## CRediT authorship contribution statement

**S. Ahmadi:** Conceptualization, Methodology, Software, Validation, Visualization, Data curation, Formal analysis, Investigation, Resources, Writing - original draft, Visualization. **P. Burgholzer:** Conceptualization, Methodology, Software, Project administration, Supervision, Funding acquisition, Validation, Resources. **P. Jung:** Methodology, Software, Formal analysis, Supervision. **G. Caire:** Supervision, Formal analysis, Project administration. **M. Ziegler:** Conceptualization, Methodology, Software, Validation, Writing - review & editing, Supervision, Software, Validation, Project administration, Resources.

## Acknowledgments

The work of P. Burgholzer was supported by the Austrian research funding association (FFG) under the scope of the COMET programm within the research project Photonic Sensing for Smarter Processes (PSSP) (contract number 871974). This programm is promoted by BMK, BMDW, the federal state of Upper Austria and the federal state of Styria, represented by SFG.

## References

[1] Burgholzer et al P. Three-dimensional thermographic imaging using a virtual wave concept. J Appl Phys 2017;121(10).
[2] Mayr et al G. Parameter estimation from pulsed thermography data using the virtual wave concept. NDT & E International 2018;100:101–7.
[3] Thiel et al E. Subsurface defect localization by structured heating using laser projected photothermal thermography. Journal of Visualized Experiments 2017(123).
[4] Puthiyaveettil N, Thomas KR, Unnikrishnakurup S, Myrach P, Ziegler M, Balasubramaniam K. Laser line scanning thermography for surface breaking crack detection: modeling and experimental study. Infrared Physics & Technology 2020;104:103141.
[5] Gustafsson MGL. Surpassing the lateral resolution limit by a factor of two using structured illumination microscopy.. J Microsc 2000;198 Pt 2:82–7.
[6] Lu J, Min W, Conchello J-A, Xie XS, Lichtman JW. Super-resolution laser scanning microscopy through spatiotemporal modulation. Nano Letters 2009;9(11):3883–9. doi:10.1021/nl902087d. PMID: 19743870
[7] Sakagami T, Matsumoto T, Kubo S, Sato D. Nondestructive testing by super-resolution infrared thermography. In: Thermosense XXXI, 7299. International Society for Optics and Photonics; 2009. p. 72990V.
[8] Irani M, Peleg S. Improving resolution by image registration. CVGIP: Graphical models and image processing 1991;53(3):231–9.
[9] Burgholzer et al P. Blind structured illumination as excitation for super-resolution photothermal radiometry. Quant Infrared Thermogr J 2019:1–11.
[10] Li et al T. Crack imaging by scanning laser-line thermography and laser-spot thermography. Measurement Science and Technology Journal 2011;22(3).
[11] Schlichting J, Ziegler M, Dey A, Maierhofer C, Kreutzbruck M. Efficient data evaluation for thermographic crack detection. Quant Infrared Thermogr J 2011;8(1):119–23.
[12] Ahmadi et al S. Photothermal super resolution imaging: a comparison of different thermographic reconstruction techniques. NDT & E International Journal 2020. doi:10.1016/j.ndteint.2020.102228.
[13] Cole et al KD. Heat conduction using Green's functions. 2nd. CRC Press; 2010.
[14] Burgholzer et al P. Super-resolution thermographic imaging using blind structured illumination. Appl Phys Lett 2017;111(3).
[15] Donoho et al D. Compressed sensing. IEEE Trans Inf Theory 2006;52(4).
[16] Haltmeier et al M. Compressed sensing and sparsity in photoacoustic thermography. J Opt 2016;18(11).
[17] Thiel E, Ziegler M, Studemund T. Localization of subsurface defects in uncoated aluminum with structured heating using high-power vcsel laser arrays. Int J Thermophys 2019;40:1–13.
[18] Zubair et al SM. Temperature solutions due to time-dependent moving-line-heat sources. Heat Mass Transfer 1996;31:185–9.
[19] Haltmeier M. Block-sparse analysis regularization of ill-posed problems via l 2, 1-minimization. In: 2013 18th International Conference on Methods & Models in Automation & Robotics (MMAR). IEEE; 2013. p. 520–3.
[20] Murray et al TW. Super-resolution photoacoustic microscopy using blind structured illumination. Optica 2017;4(1).
[21] Beck et al A. A fast iterative shrinkage-thresholding algorithm for linear inverse problems. SIAM Journal Imaging Sciences 2009;2(1).
[22] Wahba G. A comparison of gcv and gml for choosing the smoothing parameter in the generalized spline smoothing problem. The Annals of Statistics 1985;13(4):1378–402.
[23] Hansen PC, O'Leary DP. The use of the l-curve in the regularization of discrete ill–posed problems. SIAM journal on scientific computing 1993;14(6):1487–503.
[24] Mead JL. Parameter estimation: a new approach to weighting a priori information. J Inv Ill-posed Problems 2008;16(2):175–94.
[25] Burgholzer P. Thermodynamic limits of spatial resolution in active thermography. Int J Thermophys 2015;36(9):2328–41.